

Host ANP32A mediates the assembly of the influenza virus replicase

<https://doi.org/10.1038/s41586-020-2927-z>

Received: 7 February 2020

Accepted: 1 September 2020

Published online: 18 November 2020

 Check for updates

Loïc Carrique^{1,6}, Haitian Fan^{2,6}, Alexander P. Walker^{2,6}, Jeremy R. Keown^{1,6}, Jane Sharps², Ecco Staller^{3,5}, Wendy S. Barclay³, Ervin Fodor^{2,7}✉ & Jonathan M. Grimes^{1,4,7}✉

Aquatic birds represent a vast reservoir from which new pandemic influenza A viruses can emerge¹. Influenza viruses contain a negative-sense segmented RNA genome that is transcribed and replicated by the viral heterotrimeric RNA polymerase (FluPol) in the context of viral ribonucleoprotein complexes^{2,3}. RNA polymerases of avian influenza A viruses (FluPolA) replicate viral RNA inefficiently in human cells because of species-specific differences in acidic nuclear phosphoprotein 32 (ANP32), a family of essential host proteins for FluPol activity⁴. Host-adaptive mutations, particularly a glutamic-acid-to-lysine mutation at amino acid residue 627 (E627K) in the 627 domain of the PB2 subunit, enable avian FluPolA to overcome this restriction and efficiently replicate viral RNA in the presence of human ANP32 proteins. However, the molecular mechanisms of genome replication and the interplay with ANP32 proteins remain largely unknown. Here we report cryo-electron microscopy structures of influenza C virus polymerase (FluPolC) in complex with human and chicken ANP32A. In both structures, two FluPolC molecules form an asymmetric dimer bridged by the N-terminal leucine-rich repeat domain of ANP32A. The C-terminal low-complexity acidic region of ANP32A inserts between the two juxtaposed PB2 627 domains of the asymmetric FluPolA dimer, suggesting a mechanism for how the adaptive PB2(E627K) mutation enables the replication of viral RNA in mammalian hosts. We propose that this complex represents a replication platform for the viral RNA genome, in which one of the FluPol molecules acts as a replicase while the other initiates the assembly of the nascent replication product into a viral ribonucleoprotein complex.

The influenza virus genome is composed of negative-sense single-stranded RNA segments, which are assembled into separate viral ribonucleoprotein (vRNP) complexes with FluPol, a heterotrimeric complex of PB1, PB2 and PA (P3 in influenza C virus) proteins, and the viral nucleoprotein (NP)^{2,3}. Following virus entry, vRNPs are trafficked to the cell nucleus where FluPol, in complex with various host factors, directs the transcription and replication of the viral genome⁵. For replication, FluPol first generates complementary RNA (cRNA), which then serves as template for viral RNA (vRNA) synthesis. The molecular details of the replicase complex and, in particular, the role of the ANP32 family of host proteins, known to be essential for genome replication⁶, remain unknown. Here we investigate the role of ANP32A in promoting FluPol function and uncover a complex of ANP32A with a FluPol dimer, which we propose acts as a replication platform for the viral genome.

ANP32A forms a complex with a FluPol dimer

Host ANP32 proteins are essential for the activity of FluPol of both influenza A and influenza B viruses^{7,8}. To address whether FluPol from influenza C virus also requires ANP32 proteins, we performed

minigenome assays in human cells lacking ANP32A and ANP32B (Extended Data Fig. 1). No detectable FluPol activity was observed in the double-knockout cells, but expression of human ANP32A (huANP32A), human ANP32B (huANP32B) or chicken ANP32A (chANP32A) restored FluPolC activity. We then used cryo-electron microscopy (cryo-EM) to solve the structures of FluPolC in complex with huANP32A and chANP32A at a resolution ranging from 3.0 Å to 3.6 Å (Fig. 1a, b, Extended Data Figs. 2, 3, Extended Data Table 1, Supplementary Video 1). In these structures, two heterotrimeric FluPolC molecules assemble into an asymmetric dimer with the N-terminal leucine-rich repeat domain of ANP32A (ANP32A^{LRR})⁹ bridging the two FluPolC molecules. The C-terminal low-complexity acidic region of ANP32A (ANP32A^{LCAR}) could not be fully resolved in the structures. The structures of FluPolC dimers with huANP32A and chANP32A are largely identical, exhibiting the same FluPolC–FluPolC and FluPolC–ANP32A^{LRR} interaction interfaces. About 22% of particles in the FluPolC–chANP32A dataset lack density for ANP32A and were used to reconstruct a 3.4 Å resolution polymerase-only structure, which shows the same arrangement of FluPolC dimer as the ANP32A-containing complexes (Fig. 1c, Extended Data Figs. 2 and 3, Extended Data Table 1).

¹Division of Structural Biology, University of Oxford, Oxford, UK. ²Sir William Dunn School of Pathology, University of Oxford, Oxford, UK. ³Section of Molecular Virology, Imperial College London, London, UK. ⁴Diamond Light Source Ltd, Harwell Science and Innovation Campus, Didcot, UK. ⁵Present address: Sir William Dunn School of Pathology, University of Oxford, Oxford, UK. ⁶These authors contributed equally: Loïc Carrique, Haitian Fan, Alexander P. Walker, Jeremy R. Keown. ⁷These authors jointly supervised this work: Jonathan M. Grimes, Ervin Fodor.

✉e-mail: ervin.fodor@path.ox.ac.uk; jonathan@strubi.ox.ac.uk

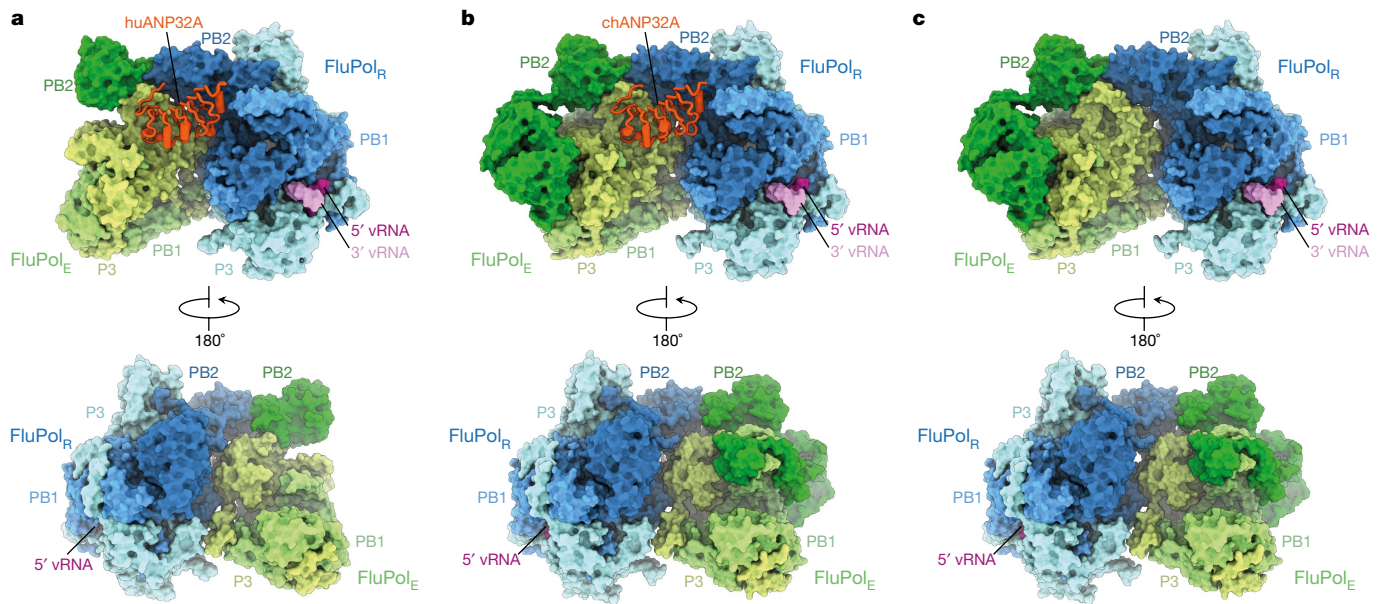


Fig. 1 | Structures of dimers of FluPolC heterotrimers with or without bound ANP32A. a–c, Cryo-EM structures of dimers of FluPolC heterotrimers with huANP32A (a) or chANP32A (b), and without ANP32A (c).

FluPol forms an asymmetric dimer

The first FluPol molecule (hereafter designated as the FluPol replicase, FluPol_R) is fully resolved in the density map and shows a configuration of the peripheral flexible domains that is distinct from the one in the cap-snatching competent transcriptase, but similar to the configuration previously observed for RNA-free FluPol and FluPol bound to cRNA^{10,11} (Fig. 1, Extended Data Fig. 4, Supplementary Video 1). Specifically, the cap-binding domain of PB2 (PB2^{cap}) is immobilized through extensive contacts with the palm subdomain of PB1, while the nuclear localization signal domain of PB2 (PB2^{NLS}) intimately associates with the N-terminal endonuclease domain of P3 (P3^{endo}). The 627 domain of PB2 (PB2⁶²⁷), named after the host-specific amino acid residue 627, makes relatively few contacts with the rest of FluPol_R. FluPol_R is bound to a 47-nucleotide long vRNA, whose 5' terminus is clearly resolved and shows the typical hook structure bound in a pocket formed by P3 and PB1, as observed previously^{12,13} (Fig. 1, Extended Data Fig. 5). In the majority of particles, the 3' vRNA terminus cannot be resolved, but the density observed around the template entry channel suggests that it has entered the active site. In about 10% of FluPolC–chANP32A and about 7% of FluPolC–huANP32A particles, the 3' vRNA terminus is bound at the interface of the C-terminal domain of P3, the thumb subdomain of PB1 and the N1 subdomain of PB2, as recently described for FluPolA and influenza D FluPol^{12,14,15}. The second FluPol molecule (hereafter designated as the encapsidating FluPol, FluPol_E) shows a markedly different configuration of the flexible domains. The C-terminal flexible domains of PB2 (PB2^{cap}, PB2 mid-link domain (PB2^{mid-link}), PB2⁶²⁷ and PB2^{NLS}) flip over to pack against the C-terminal domain of the P3 subunit (P3^{CTD}) (Extended Data Fig. 4, Supplementary Video 1). P3^{endo}, several N-terminal domains of PB2 and the C-terminal 18 amino acid residues of PB2^{NLS} are disordered in FluPol_E. Furthermore, approximately 52% of FluPolC–chANP32A and all FluPolC–huANP32A particles lack density for PB2^{cap} and PB2^{mid-link} in FluPol_E, suggesting that these domains are flexible. No RNA was found associated with FluPol_E. The two FluPolC molecules make extensive interactions, mainly between their respective PB2 and P3 subunits, to form a large polymerase dimer interface burying a total of ~1,500 Å² (Fig. 2a). The PB2⁶²⁷ domain of FluPol_R interacts with the P3^{CTD}, PB2⁶²⁷ and PB2^{NLS}

domains of FluPol_E (Fig. 2b), and the P3^{CTD} domain of FluPol_E stacks against the PB2 N2 (PB2^{N2}) and PB2^{mid-link} domains of FluPol_R (Fig. 2c). In addition, the P3 arch and PB1 β-hairpin of FluPol_E contact the P3^{CTD} and PB2^{N2} domains of FluPol_R (Fig. 2d). This dimer interface is distinct from the one observed previously in FluPolA, which promotes template realignment and is required for replication initiation on a cRNA^{12,16}. To address the functional relevance of this dimer interface in influenza A virus, we introduced alanine mutations to several clusters of amino acid residues in FluPolA located at or close to the dimer interface on the basis of the structure of the FluPolC heterotrimeric dimer. These include the residues PA K324/H326/E327, PA K339/Q340 and PB2 P132, which are structurally equivalent to P3 R299/K301/D302, P3 N318/Q319 and PB2 E139 in FluPolC, respectively (Supplementary Fig. 1). All of these mutations resulted in a reduction of viral RNA levels in a minigenome assay analysing FluPol function (Extended Data Fig. 6a). These data indicate that amino acid residues at the asymmetric FluPol dimer interface we have identified in the FluPolC–ANP32A complexes are important for FluPol activity.

ANP32A^{LRR} bridges the asymmetric FluPol dimer

In both the FluPolC–huANP32A and FluPolC–chANP32A structures, the ANP32A^{LRR} domain binds in a depression formed by the FluPolC dimer interface (Figs. 1a, b, 2e, Supplementary Video 1). The N-terminal region of ANP32A^{LRR} interacts with FluPol_R, involving multiple regions of PB2, including the lid domain (PB2^{lid}), PB2⁶²⁷ and PB2^{NLS} (Fig. 2e, f). These interactions bury a total of about 600 Å² at the interface between ANP32A and FluPol_R. The C-terminal region of ANP32A^{LRR} interacts with the P3^{CTD} domain and the N terminus of PB1 of FluPol_E, and buries a total of about 490 Å² at the interface (Fig. 2e, g, h). ANP32A N129 and D130, previously identified as important for FluPolA binding and activity^{8,17}, are directly involved in the interaction with FluPol_E. Specifically, N129 is sandwiched between M387 and K391 of P3 and interacts with K391 directly through hydrogen bonding, whereas D130 interacts with K608 of P3 (Fig. 2g). To address the functional relevance of this interaction, we mutated PA K413 in FluPolA—equivalent to P3 K391 in FluPolC (Fig. 2g, Supplementary Fig. 1)—to alanine. This mutant FluPolA showed reduced binding to huANP32A and loss of activity in a minigenome assay (Extended Data

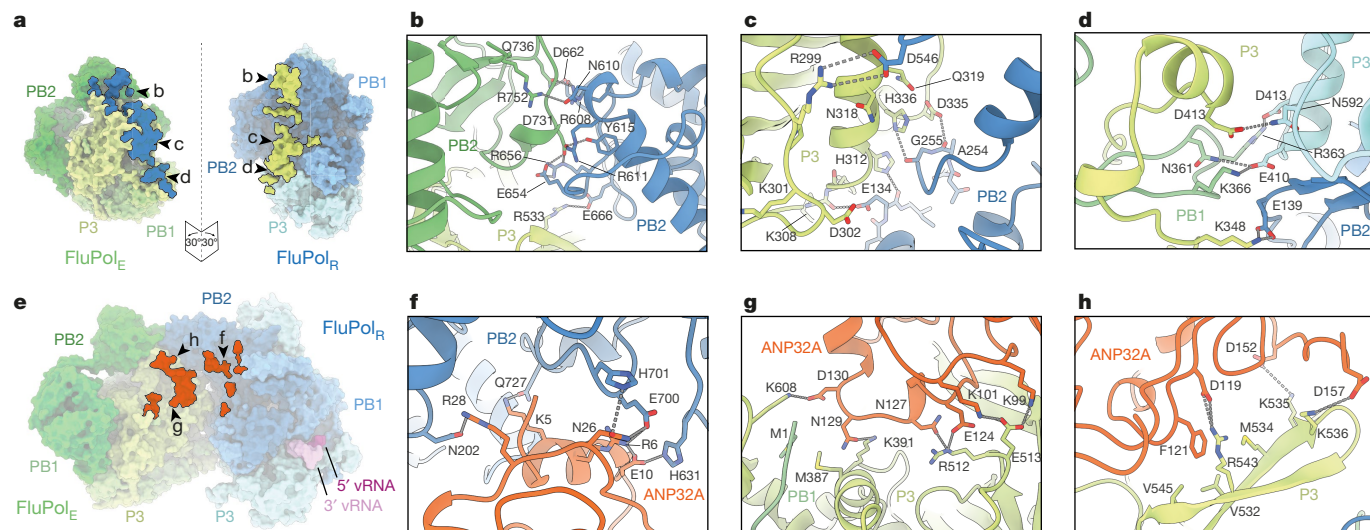


Fig. 2 | FluPolC–FluPolE and ANP32A–FluPolC interaction interfaces. **a**, The FluPolC–FluPolE dimer interface with interacting regions in FluPol_R and FluPol_E highlighted on the molecular surface; the two molecules are shown peeled apart by 30° to highlight the surface. Letters denote the close-up views shown in **b–d**. **b–d**, Close-up views of the FluPolC–FluPolE interaction interface

indicated in **a**. Dashed lines indicate hydrogen bonds. **e**, ANP32A–FluPolC interface with interacting regions in FluPolC highlighted. Letters denote the close-up views shown in **f–h**. **f–h**, Close-up views of the ANP32A–FluPolC interaction interface indicated in **e**. Dashed lines indicate hydrogen bonds.

Fig. 7). Further mutations in FluPolA at PA D529 and PB2 T609, corresponding to P3 E513 and PB2 H631 in FluPolC (Fig. 2f, g, Supplementary Fig. 1), had similar inhibitory effects on both ANP32A binding and FluPol activity. Together, these data confirm the functional relevance of the identified ANP32A–FluPol interaction and provide an explanation for why chicken ANP32B (chANP32B) with I129 and N130 is unable to support FluPol activity^{8,17}.

ANP32A^{LCAR} interacts with PB2⁶²⁷

Species-specific differences in ANP32 proteins underpin the low activity of avian FluPolA in mammalian cells⁴. Amino acid differences important for FluPol activity have been identified in both ANP32A^{LRR} and ANP32A^{LCAR}, but a 33-amino-acid insertion in the avian ANP32A^{LCAR} relative to mammalian ANP32A^{LCAR} was found to be the most critical for the ability of avian ANP32A to support the activity of avian FluPolA^{4,18,19} (Fig. 3a). Although the ANP32A^{LCAR} could not be assigned unambiguously in the map, continuous density shows that it contacts PB2⁶²⁷ of FluPol_R (Fig. 3b, c, Supplementary Video 2). These data are in agreement with previous reports of a direct interaction between ANP32A and the PB2⁶²⁷ domain using biochemical methods and NMR^{20–22}. In the FluPolC–chANP32A structure, the negatively charged chANP32A^{LCAR} binds in a basic groove formed by the PB2⁶²⁷ domains of FluPol_R and FluPol_E, with the avian-specific 33-amino-acid insertion directly contacting the PB2⁶²⁷ domain of FluPol_R. This interaction positions a previously identified hydrophobic SUMO interaction motif-like sequence²³ (Extended Data Fig. 1c) on top of PB2⁶²⁷, as well as a downstream region of the ANP32^{LCAR} which contains a mixture of basic and acidic amino acid residues (176-VLSLVKDR-183) (Fig. 3a–c). Specifically, this motif is located next to PB2 K649 (equivalent to E627 in the PB2 of avian FluPolA) and V614. PB2 V614 is equivalent to K591 in the 2009 H1N1 pandemic influenza A virus, which was of swine origin, and retained E627 in its avian PB2 but used a Q591K adaptation to increase polymerase activity^{24,25} (Extended Data Fig. 8, Supplementary Fig. 1). Interaction of this region of ANP32A with PB2⁶²⁷ could be critical for stabilization of the interaction between ANP32A and FluPol and, consequently, for the ability of ANP32A to support FluPol activity. The presence of a mixture of basic and acidic amino acid residues in this region could explain why avian ANP32A is able to support FluPol with

either avian-specific 627E or mammalian-specific 627K in PB2. The corresponding region in huANP32A (176-EEEYDEDA-183), as well as in the huANP32B isoform (176-DEEDEDDE-183), is entirely acidic (Fig. 3a), potentially explaining the need to eliminate the acidic residue 627 in avian FluPolA upon viral transmission to a mammalian host. To test this hypothesis, we replaced the acidic 176–183 region of huANP32A with the corresponding region from chANP32A and found that this mutant form of huANP32A was able to fully support the activity of FluPolA with 627E in mammalian cells (Fig. 3d). These data are also in agreement with a previous study reporting that FluPolA can tolerate a range of non-acidic amino acid residues at position 627 and activity is positively correlated with the pI value of the amino acid²⁶. Thus, our data provide an explanation for adaptive mutations observed in FluPolA upon transmission of influenza A virus from an avian to a human host.

Implications for genome replication

The product exit channel of vRNA-bound FluPol_R, located along the PB1 finger domains and PB2^{cap}, points towards the 5′-cRNA binding site of FluPol_E, which is located next to the PA arch (residues 343–376) and the PB1 β-hairpin (residues 353–370)^{13,15}. A path lined with basic amino acid residues connects this exit channel with the 5′-cRNA binding site of FluPol_E (Fig. 4a, Supplementary Video 3) and FluPol_E is thus ideally positioned to capture the 5′ end of a nascent cRNA product emerging from the active site of FluPol_R. This suggests that in the FluPolC–ANP32A complex, FluPol_R functions as the replicase, whereas FluPol_E acts as an ‘encapsidating’ polymerase, initiating the co-replicative assembly of the nascent cRNA with NP into a complementary ribonucleoprotein (cRNP) complex. To test this hypothesis, we performed a cRNA-stabilization assay²⁷ to examine the ability of FluPol to encapsidate nascent cRNA product. Mutations in FluPol_E at PA K324/H326/E327 and PA K339/Q340 caused a substantial reduction in cRNA accumulation. Note that PB2 P132 is located on the FluPol_R side of the interface and therefore this mutation could not be tested using this assay. These data confirm that the FluPol_R–FluPol_E interface is important for encapsidation of a nascent cRNA product (Extended Data Fig. 6b). The PB2⁶²⁷ domain of FluPol_E has been implicated in cRNA encapsidation using this assay, which is consistent with our model²⁸.

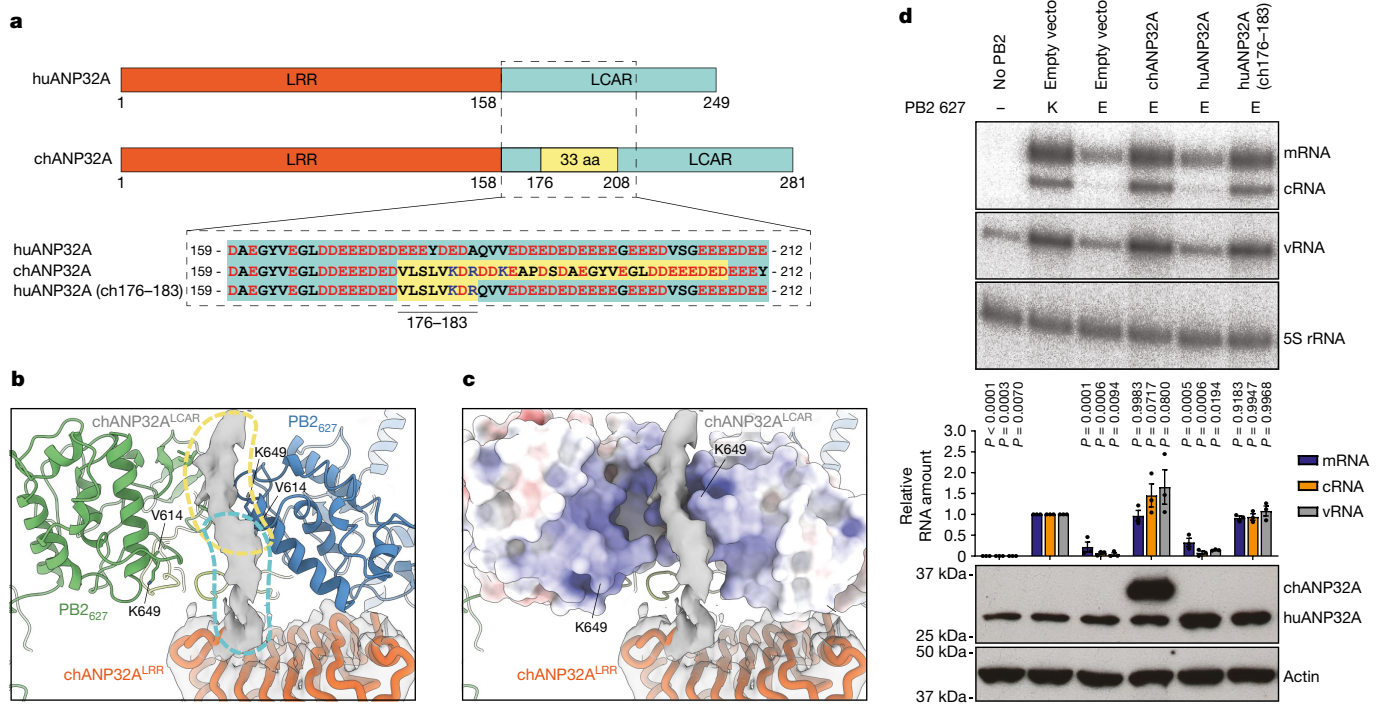


Fig. 3 | Interaction of ANP32^{LCAR} with FluPolC and the effect of ANP32A on FluPolA activity. **a**, Schematic of huANP32A and chANP32A, highlighting the 33-amino-acid insertion (33 aa) (yellow) in chANP32A and sequence differences. huANP32A(ch176–183) is a huANP32A construct in which residues 176–183 are replaced by those from chANP32A. Acidic and basic amino acid residues are highlighted in red and blue, respectively. **b**, Close-up view of the cryo-EM density attributed to chANP32A (grey, threshold 0.934) with the chANP32A^{LRR} domain represented in cartoon (orange) and the positions of PB2⁶²⁷ of FluPol_R (blue) and FluPol_E (green). Regions potentially corresponding to the N-terminal part of ANP32A^{LCAR} and part of the avian 33-amino-acid insertion are highlighted in cyan and yellow, respectively. V614 and K649 in FluPolC correspond to K591 (Q) and K627 (E) in FluPolA (residues in

parentheses are avian species-specific), respectively. **c**, Same view as shown in **b**, with PB2⁶²⁷ of FluPol_R and FluPol_E shown in surface representation. **d**, Effect of wild-type chANP32A and huANP32A, and huANP32A(ch176–183) on the activity of FluPolA with mammalian-adapted PB2⁶²⁷ or avian-signature PB2^{E627} in a vRNP-reconstitution assay in mammalian HEK 293T cells. Top, primer-extension analysis of viral RNA levels with quantification. Bottom, western blot analysis of ANP32A levels with molecular weight markers. Data are mean ± s.e.m., *n* = 3 biologically independent samples from 3 independent experiments. Ordinary one-way ANOVA with Dunnett's post hoc test for multiple comparisons. *P* < 0.05 is considered significant to reject the null hypothesis. Gel source data are presented in Supplementary Fig. 2.

We propose that a similar mechanism is likely to apply for cRNA-bound FluPol_R, owing to intrinsic similarities between cRNA synthesis and vRNA synthesis, which both require co-replicative encapsidation of nascent RNA.

Such a role for the FluPol–ANP32A complex in viral genome replication is consistent with previous observations; in particular, ANP32A and the adaptive PB2 E627K mutation have been specifically linked to viral genome replication rather than transcription^{7,29,30} providing strong support for a role of the FluPol–ANP32A complex in replication. We were unable to fully resolve ANP32A^{LCAR} in our structures, indicating that this part of ANP32A is highly dynamic. Replication involves viral NP, which co-replicatively coats viral RNA along its length, but it is currently unknown how NP is recruited onto the growing nascent chain of RNA. Non-segmented negative-strand RNA viruses encode an acidic phosphoprotein (P) that is an essential component of their RNA polymerase complex and is involved in recruiting NP to nascent replication product³¹. Segmented negative-strand RNA viruses do not encode an equivalent protein and it is tempting to speculate that its function is performed by a cellular protein such as ANP32A. Specifically, the unstructured region of ANP32A^{LCAR}, downstream of the region interacting with FluPol_R, could act as a molecular whip recruiting NP in a manner analogous to that proposed for the P phosphoprotein.

Understanding the structural basis for why ANP32A is fundamental to influenza virus replication opens a new perspective on the role of ANP32A and host-adaptive mutations in FluPol function.

Specifically, our data suggest that the FluPol–ANP32A complex represents a replication platform for the influenza virus RNA genome. The mechanistic insights gained from this study have enabled us to build a more complete picture of the structural basis for the viral replication cycle. During infection, incoming vRNPs bind to the C-terminal domain of host RNA polymerase II through interactions primarily mediated by the C-terminal domain of FluPol PA^{32,33}. This interaction stabilizes FluPol in a cap-snatching-competent conformation, enabling the cleavage of host capped RNAs that serve as primers for the initiation of viral mRNA synthesis³³. Accumulation of newly synthesized FluPol favours genome replication over transcription, consistent with a transition from transcription to replication as infection proceeds, through forming an asymmetric dimer with the vRNP-associated resident FluPol and stabilizing it in a replication-competent conformation, enabling primer-independent initiation of replication (Fig. 4). ANP32A contributes to the stabilization of this dimer by bridging the two FluPol molecules. Several lines of evidence suggest that ANP32A is involved in cRNA-to-vRNA replication, although there is also evidence in favour of a role during vRNA-to-cRNA replication^{7,18,29,30}. In particular, avian polymerase in human cells is incapable of generating replication-competent cRNPs, suggesting that cRNA encapsidation—and hence the correct assembly of cRNPs—might be affected²⁹; this is fully consistent with our data showing that mutations at the FluPol_R–FluPol_E dimer interface interfere with cRNA encapsidation. ANP32A may have a particularly important role in stabilizing the interaction of a free

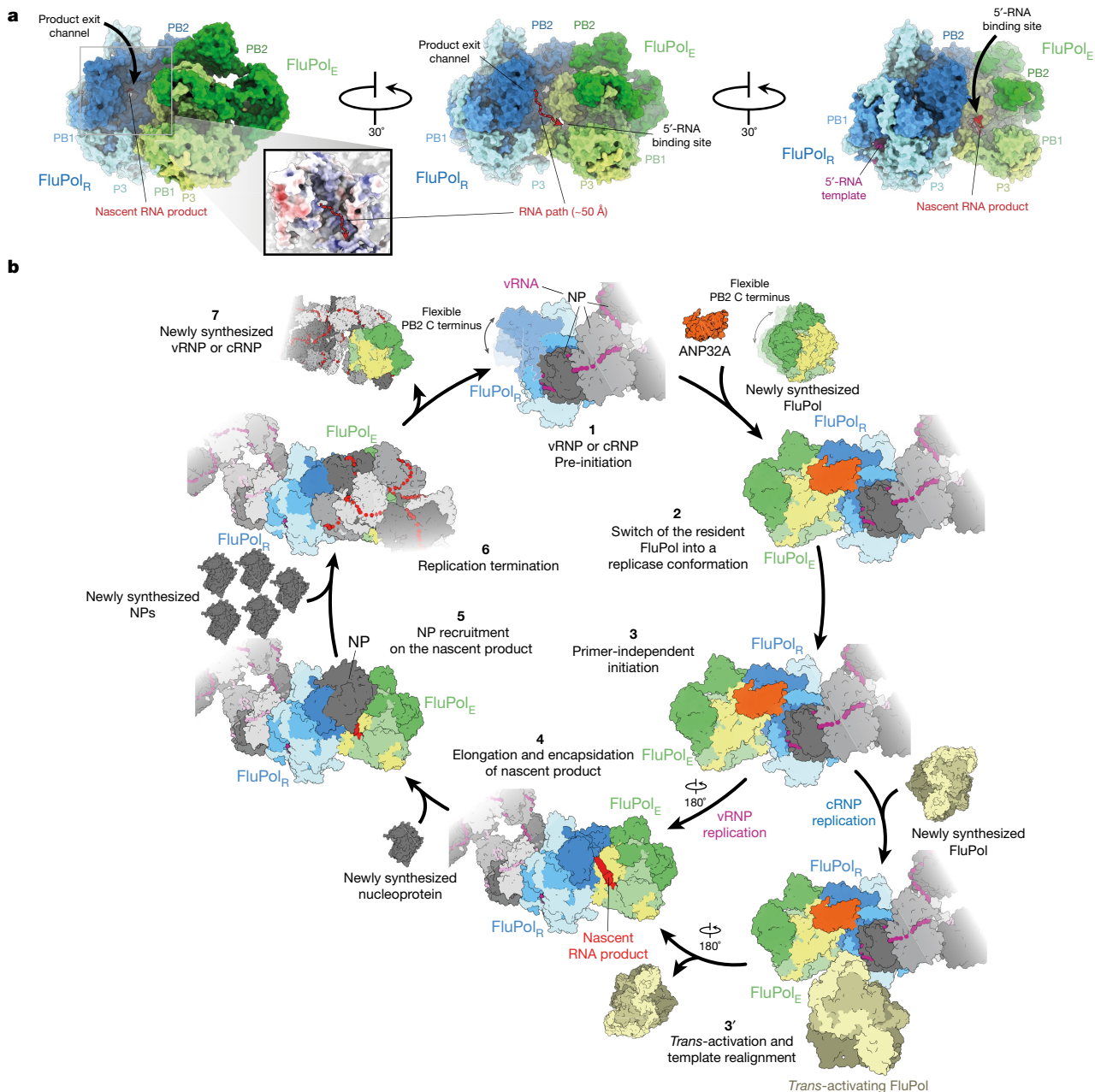


Fig. 4 | Functional implications of the FluPolC–ANP32A complex. **a**, Relative positions of the RNA-product exit channel in FluPol_R and the 5'-RNA binding site in FluPol_E in the chANP32A–FluPolC complex. The positions of the RNA-product exit channel in FluPol_R and the 5'-RNA binding site in FluPol_E were determined by superposing FluPol_R and FluPol_E with the structure of FluPolA bound to capped RNA and vRNA template (Protein Data Bank (PDB): 6RR7). **b**, Model for the role of FluPol–ANP32A complex in the replication of the influenza virus RNA genome and its assembly into vRNPs. FluPol in the context of vRNP or cRNP is flexible (1) but is stabilized in a replicase FluPol_R conformation upon binding of a newly synthesized FluPol in the presence of

ANP32A (2). FluPol_R initiates replication in a primer-independent manner (3), with a *trans*-activating FluPol involved in cRNA to vRNA replication by promoting cRNA template realignment (3'). As the 5' end of the nascent replication product is released from the polymerization active site of FluPol_R, it is captured in the 5'-RNA binding pocket of the encapsidating FluPol_E bound to FluPol_R (4), initiating the encapsidation of the nascent RNA with NP (5). Nascent vRNA or cRNA assemble into vRNPs or cRNPs, respectively (6), and are released upon FluPol_R termination. FluPol_E becomes the resident polymerase of the newly produced vRNP or cRNP.

FluPol with a cRNP-associated FluPol, as cRNPs need to make at least two different interactions with free FluPol molecules using two different interaction interfaces, to promote template realignment and nascent-product encapsidation. These interactions need to be fine-tuned in a host-dependent manner, in agreement with the observation of adaptive mutations at the dimer interfaces^{12,34}. Dependence on free FluPol to ensure template realignment during replication initiation on a cRNA template¹² and co-replicative

genome assembly into a vRNP both provide the virus with a safety mechanism to avoid the generation of naked viral RNA in the absence of viral protein synthesis, which could otherwise be a trigger for activating innate immune responses³⁵. The identification of amino acid residues involved in mediating ANP32A–FluPol interactions will facilitate both the development of novel small-molecule inhibitors that disrupt the interaction interface and the design of genetically engineered animals resilient to influenza virus.

Online content

Any methods, additional references, Nature Research reporting summaries, source data, extended data, supplementary information, acknowledgements, peer review information; details of author contributions and competing interests; and statements of data and code availability are available at <https://doi.org/10.1038/s41586-020-2927-z>.

- Krammer, F. et al. Influenza. *Nat. Rev. Dis. Primers* **4**, 3 (2018).
- Fodor, E. & Te Velhuis, A. J. W. Structure and function of the influenza virus transcription and replication machinery. *Cold Spring Harb. Perspect. Med.* **10**, a038398 (2019).
- Wandzik, J. M., Kouba, T. & Cusack, S. Structure and function of influenza polymerase. *Cold Spring Harb. Perspect. Med.* **10**, a038372 (2020).
- Long, J. S. et al. Species difference in ANP32A underlies influenza A virus polymerase host restriction. *Nature* **529**, 101–104 (2016).
- Walker, A. P. & Fodor, E. Interplay between influenza virus and the host RNA polymerase II transcriptional machinery. *Trends Microbiol.* **27**, 398–407 (2019).
- Peacock, T. P., Sheppard, C. M., Staller, E. & Barclay, W. S. Host determinants of influenza RNA synthesis. *Annu. Rev. Virol.* **6**, 215–233 (2019).
- Staller, E. et al. ANP32 proteins are essential for influenza virus replication in human cells. *J. Virol.* **93**, e00217-19 (2019).
- Zhang, H. et al. Fundamental contribution and host range determination of ANP32A and ANP32B in influenza A virus polymerase activity. *J. Virol.* **93**, e00174-19 (2019).
- Huyton, T. & Wolberger, C. The crystal structure of the tumor suppressor protein pp32 (Anp32a): structural insights into Anp32 family of proteins. *Protein Sci.* **16**, 1308–1315 (2007).
- Hengrung, N. et al. Crystal structure of the RNA-dependent RNA polymerase from influenza C virus. *Nature* **527**, 114–117 (2015).
- Thierry, E. et al. Influenza polymerase can adopt an alternative configuration involving a radical repacking of PB2 domains. *Mol. Cell* **61**, 125–137 (2016).
- Fan, H. et al. Structures of influenza A virus RNA polymerase offer insight into viral genome replication. *Nature* **573**, 287–290 (2019).
- Pflug, A., Guilligay, D., Reich, S. & Cusack, S. Structure of influenza A polymerase bound to the viral RNA promoter. *Nature* **516**, 355–360 (2014).
- Peng, Q. et al. Structural insight into RNA synthesis by influenza D polymerase. *Nat. Microbiol.* **4**, 1750–1759 (2019).
- Wandzik, J.M. et al. A structure-based model for the complete transcription cycle of influenza polymerase. *Cell* **181**, 877–893 (2020).
- Chang, S. et al. Cryo-EM structure of influenza virus RNA polymerase complex at 4.3 Å resolution. *Mol. Cell* **57**, 925–935 (2015).
- Long, J. S. et al. Species specific differences in use of ANP32 proteins by influenza A virus. *eLife* **8**, e45066 (2019).
- Bi, Z. et al. Insights into species-specific regulation of ANP32A on the mammalian-restricted influenza virus polymerase activity. *Emerg. Microbes Infect.* **8**, 1465–1478 (2019).
- Zhang, H. et al. A unique feature of swine ANP32A provides susceptibility to avian influenza virus infection in pigs. *PLoS Pathog.* **16**, e1008330 (2020).
- Baker, S.F., Ledwith, M.P. & Mehle, A. Differential splicing of ANP32A in birds alters its ability to stimulate rna synthesis by restricted influenza polymerase. *Cell Rep.* **24**, 2581–2588 (2018).
- Camacho-Zarco, A. R. et al. Molecular basis of host-adaptation interactions between influenza virus polymerase PB2 subunit and ANP32A. *Nat. Commun.* **11**, 3656 (2020).
- Mistry, B. et al. Elucidating the interactions between influenza virus polymerase and host factor ANP32A. *J. Virol.* **94**, e01353-19 (2020).
- Domingues, P. & Hale, B. G. Functional insights into ANP32A-dependent influenza A virus polymerase host restriction. *Cell Rep.* **20**, 2538–2546 (2017).
- Mehle, A. & Doudna, J. A. Adaptive strategies of the influenza virus polymerase for replication in humans. *Proc. Natl Acad. Sci. USA* **106**, 21312–21316 (2009).
- Yamada, S. et al. Biological and structural characterization of a host-adapting amino acid in influenza virus. *PLoS Pathog.* **6**, e1001034 (2010).
- Chin, A. W. H. et al. Influenza A viruses with different amino acid residues at PB2-627 display distinct replication properties in vitro and in vivo: revealing the sequence plasticity of PB2-627 position. *Virology* **468–470**, 545–555 (2014).
- Vreede, F. T., Jung, T. E. & Brownlee, G. G. Model suggesting that replication of influenza virus is regulated by stabilization of replicative intermediates. *J. Virol.* **78**, 9568–9572 (2004).
- Nilsson, B. E., Te Velhuis, A. J. W. & Fodor, E. Role of the PB2 627 domain in influenza A virus polymerase function. *J. Virol.* **91**, e02467-16 (2017).
- Mänz, B., Brunotte, L., Reuther, P. & Schwemmler, M. Adaptive mutations in NEP compensate for defective H5N1 RNA replication in cultured human cells. *Nat. Commun.* **3**, 802 (2012).
- Sugiyama, K., Kawaguchi, A., Okuwaki, M. & Nagata, K. pp32 and APRIL are host cell-derived regulators of influenza virus RNA synthesis from cRNA. *eLife* **4**, e08939 (2015).
- Pan, J. et al. Structure of the human metapneumovirus polymerase phosphoprotein complex. *Nature* **577**, 275–279 (2020).
- Lukarska, M. et al. Structural basis of an essential interaction between influenza polymerase and Pol II CTD. *Nature* **541**, 117–121 (2017).
- Serna Martin, I. et al. A mechanism for the activation of the influenza virus transcriptase. *Mol. Cell* **70**, 1101–1110 (2018).
- Chen, K. Y., Santos Afonso, E. D., Enouf, V., Ise, C. & Naffakh, N. Influenza virus polymerase subunits co-evolve to ensure proper levels of dimerization of the heterotrimer. *PLoS Pathog.* **15**, e1008034 (2019).
- Killip, M. J., Fodor, E. & Randall, R. E. Influenza virus activation of the interferon system. *Virus Res.* **209**, 11–22 (2015).

Publisher's note Springer Nature remains neutral with regard to jurisdictional claims in published maps and institutional affiliations.

© The Author(s), under exclusive licence to Springer Nature Limited 2020

Methods

No statistical methods were used to predetermine sample size. The experiments were not randomized and investigators were not blinded to allocation during experiments and outcome assessment.

Cells

Human embryonic kidney 293T (HEK 293T) and Sf9 insect cells were sourced from the Cell Bank of the Sir William Dunn School of Pathology, University of Oxford. HEK 293T cells were maintained in Dulbecco's Modified Eagle Medium (DMEM) and Sf9 cells were maintained in Sf-900 II serum free medium (Gibco). Human eHAP cells (Horizon Discovery), control or lacking ANP32A and ANP32B proteins (dKO), were cultured in Iscove's modified Dulbecco's medium (IMDM; Sigma) supplemented with 10% fetal bovine serum (FBS; Sigma), 1% nonessential amino acids (NEAA; Gibco), and 1% penicillin/streptomycin (Gibco) and have been described⁷. Cell lines have not been authenticated but tested negative for mycoplasma contamination.

Protein expression and purification

The three subunits of influenza C/Johannesburg/1/1966 virus polymerase, together with human or chicken ANP32A, were co-expressed in Sf9 cells from codon-optimized genes (GeneArt) cloned into a single baculovirus using the MultiBac system³⁶. Expression and purification of the co-expressed complex were performed as previously described^{10,12} with minor modifications: the salt concentration in all buffers was set to 150 mM to maintain FluPoIC-ANP32A complex formation. Size-exclusion chromatography was performed using 25 mM HEPES-NaOH, pH 7.5, 150 mM NaCl and 5% (v/v) glycerol on a Superdex 200 Increase 10/300 GL column (GE Healthcare).

Cryo-EM sample preparation

Protein surface charges of the purified complex were neutralized by adding 0.001% glutaraldehyde for 20 min on ice to minimize preferential orientation of particles. After quenching the reaction by adding Tris-HCl, pH 8.0 to a final concentration of 100 mM, the sample was injected onto a Superdex 200 Increase 10/300 GL column (GE Healthcare) together with a 47 nt vRNA (5'-AGUAGAAACAAGGGUUAUUUUUCUUUACUAGUCUACCCUGCUUUUGCU-3') using 25 mM HEPES-NaOH, pH 7.5, 150 mM NaCl as the running buffer. This 47-nucleotide (nt) vRNA contains the 5' and 3' promoter elements recognized and bound by FluPol. The fractions of interest were concentrated to 0.23–0.28 mg ml⁻¹ and RNA binding was confirmed by measuring the A_{260}/A_{280} ratio. A final concentration of 0.005% (v/v) Tween 20 was added before grid preparation. A volume of 3–4 μ l of sample was placed on glow-discharged Quantifoil Holey Carbon grids (R 2/1, with 2 μ m holes and 1 μ m spacing and applied on biocompatible 200 gold mesh), before blotting for 3.0–3.5 s and flash-freezing in liquid ethane. All grids were prepared using a Vitrobot mark IV (FEI) at 95–100% humidity.

Cryo-EM image collection and processing

Cryo-EM data for the FluPoIC-chANP32A sample were collected on a 300 kV Titan Krios microscope (Thermo Fisher Scientific) at the Division of Structural Biology (Strubi). Automated data collection was setup in EPU 2.1 using a K2 Summit (Gatan) direct electron detector at 1.37 \AA per pixel operating in counting mode and a GIF Quantum energy filter (Gatan) with 20 eV slit. Sample was collected with a tilt angle of 30° at a dose of $-38.8 \text{ e}^- \text{\AA}^{-2}$ across 44 frames for a dose rate of $-3.527 \text{ e}^- \text{\AA}^{-2} \text{ s}^{-1}$, using a defocus range of $-2 \text{ }\mu\text{m}$ to $-3.5 \text{ }\mu\text{m}$. Cryo-EM data for the FluPoIC-huANP32A sample were collected on a 300 kV Titan Krios microscope (Thermo Fisher Scientific) at Electron Bio-Imaging Centre (eBIC). Automated data collection was setup in SerialEM 3.7 using a K3 (Gatan) direct electron detector operating in super-resolution mode at 0.5425 \AA per pixel and a GIF Quantum energy filter (Gatan) with 20 eV slit. Sample was collected with a tilt angle of 20°

at a dose of $-32.1 \text{ e}^- \text{\AA}^{-2}$ across 34 frames for a dose rate of $-16 \text{ e}^- \text{\AA}^{-2} \text{ s}^{-1}$, using a defocus range of $-2 \text{ }\mu\text{m}$ to $-3.5 \text{ }\mu\text{m}$. Sample-specific data collection parameters are summarized in Extended Data Table 1. Data processing pipelines are shown in Extended Data Fig. 1. In brief, raw movies were processed using MotionCor2-1.1.0³⁷, with a five-by-five patch-based alignment, keeping all of the frames and dose-weighting up to the total exposure. For the K3 super-resolution, the data have been binned 2 times at the motion correction step, giving a final pixel size of 1.085 \AA per pixel. The contrast transfer function (CTF) of full-dose, non-weighted micrographs was initially estimated using Gctf-v.1.06³⁸ or cryoSPARC v.2.12.0³⁹ Patch-CTF. Poor-quality images were discarded after manual inspection. Particles were blob picked in cryoSPARC v.2.12.0³⁹ and the 2D classes were inspected and classes of interest were selected to generate templates for complete particle picking. For the FluPoIC-chANP32A dataset, a total number of 2,534,332 particles were picked and a final number of 772,989 particles were exported to RELION 3.1⁴⁰ after 2D and 3D class selection. The consensus map was refined to 3.50 \AA . Bayesian polishing and per particle CTF refinement and B-factor estimation with beam tilt correction were performed in RELION 3.1 which improved map resolution to 3.2 \AA . High order aberration and magnification anisotropy refinement improved map resolution to 3.1 \AA . Global and focus 3D classification were performed within RELION (Extended Data Fig. 2a). For the 3D variability analysis, polished particles and model were imported into cryoSPARC v.2.12.0 and refined using the non-uniform refinement job. A mask was then designed around the density corresponding to the PB2⁶²⁷ domains of both polymerases and chANP32A. The 3D variability analysis was then performed using this mask, asking for solving the three main modes on a structure low pass filtered to 6 \AA . The results of this principal component analysis were clustered in twenty sub-populations and models were reconstructed for each of the individual clusters. One cluster was showing a clear density for the chANP32A^{LCAR} region and was refined using the non-uniform refinement job to 3.6 \AA (Subclass 2). In parallel, all of the particles having a strong density for chANP32A were selected and refined using the non-uniform refinement job to 3.1 \AA . The same 3D variability analysis was performed, asking for solving the three main modes on a structure low pass filtered to 6 \AA . Mode 3 is displayed as Supplementary Video 2. For the FluPoIC-huANP32A dataset, a total number of 2,312,045 particles were picked and a final number of 835,198 particles were exported to RELION 3.1 after 2D and 3D class selection. The consensus map was refined to 3.2 \AA . Bayesian polishing and per particle CTF refinement and B-factor estimation with beam tilt correction were performed in RELION 3.1 which improved map resolution to 2.8 \AA . Global and focus 3D classification were performed within RELION (Extended Data Fig. 2b). CryoEF⁴¹ and 3D Fourier shell correlation (FSC)⁴² sphericity scores were used to confirm that the final maps were not suffering from distortion bias due to preferred specimen orientation. The structures were modelled by first fitting ANP32A^{LRR} (PDB ID: 4XOS), FluPoIC (PDB ID: 5D98) and 5' and 3' vRNA termini (PDB ID: 6RR7) using UCSF Chimera⁴³. One cycle of rigid body real space refinement followed by manual adjustment in Coot⁴⁴ was performed to correctly position the C α chain into the density. Locally sharpened maps were generated using LocScale⁴⁵ in the CCP-EM⁴⁶ package. Finally, cycles of PHENIX⁴⁷ real space refinement and manual building in Coot⁴⁴ were used to improve model geometry. Map-to-model comparison in PHENIX mtriage validated that no over-fitting was present in the structures. Model geometry was validated for all models using MolProbity⁴⁸. All map and model statistics are detailed in Extended Data Table 1. A homology model of FluPoIA-ANP32A complex structure was generated using SWISS-MODEL⁴⁹.

Plasmids

Plasmids pHMG-PB1, pHMG-PB2, pHMG-P3 and pHMG-NP expressing the subunits of FluPoIC and NP of influenza C/Johannesburg/1/66 virus and pPoll-Luci-CP3-RT expressing a luciferase reporter have

been described^{50,51}. pcDNA-PB1, pcDNA-PB1a (catalytically inactive; D445A/D446A), pcDNA-PB2, pcDNA-PB2 K627E, pcDNA-PA, pcDNA-NP and pPOLI-NA, which encodes an NA vRNA segment, are derived from influenza A/WSN/33 virus and have been described previously^{27,52–54}. pCAGGS-chANP32A has been described previously⁴. pcDNA-huANP32A and pCAGGS-huANP32A-Strep were produced from pCAGGS-huANP32A⁴ by restriction-ligation cloning. pcDNA-huANP32A(ch176-183), pcDNA-PB2 T609A, pcDNA-PB2 P132A, pcDNA-PA D529A/R531A/E533A, pcDNA-PA K413A, pcDNA-PA K324A/H326A/E327A and pcDNA-PA K339A/Q340A were generated from pcDNA-huANP32A, pcDNA-PB2 and pcDNA-PA by site-directed PCR mutagenesis and validated by Sanger sequencing.

Influenza C virus vRNP-reconstitution and luciferase-reporter assays

Approximately 0.2×10^6 eHAP cells, control or dKO, were transfected with plasmids pHMG-PB1, pHMG-PB2, pHMG-P3, pHMG-NP, pPolI-Luci-CP3-RT and pcDNA-Renilla using Lipofectamine 2000 according to the manufacturer's instructions. Where indicated, plasmids pCAGGS-huANP32A, pCAGGS-huANP32B or pCAGGS-chANP32A were included. Cells were lysed 24 h after transfection using Passive lysis buffer (Promega). Firefly and Renilla luciferase activities were measured using a Promega dual luciferase kit and firefly activity levels were normalized to the Renilla control.

Influenza A virus vRNP-reconstitution assay and primer extension analysis

Approximately 0.2×10^6 HEK 293T cells were transfected with plasmids pcDNA-PB1, pcDNA-PB2, pcDNA-PA, pcDNA-NP and pPOLI-NA using Lipofectamine 2000 according to the manufacturer's instructions. Where indicated, plasmids encoding ANP32A proteins or mutant polymerase subunits were included. Total cellular RNA was extracted 20 h after transfection using TRI reagent (Sigma) according to the manufacturer's instructions. NA segment RNA levels were assessed using primer extension⁵⁵. In brief, primers complementary to the positive (5'-TGGACTAGTGGGAGCATCAT-3') and negative (5'-TCCAGTATGTTTTGATTCCG-3') sense NA segment viral RNA species were labelled with ³²P and total cellular RNA was reverse transcribed. A primer complementary to 5S rRNA (5'-TCCCAGCGGTCTCCCATCC-3') was included as a loading control. Products were resolved by 6% denaturing PAGE and visualized by phosphorimaging. Product bands were identified by comparison with previously published data^{56,57}. Analysis was carried out using ImageJ⁵⁸ and Prism 8 (GraphPad), and viral RNA signals were normalized to the 5S rRNA loading control.

Western blotting

Western blotting of all proteins was carried out using specific rabbit polyclonal antibodies. PB1 and PB2 were blotted using commercially available antibodies (Genetex), while PA was blotted using a custom-made antibody⁵⁹. ANP32A and actin were blotted using commercially available antibodies (Sigma). In all cases the secondary antibody used was goat anti-rabbit conjugated to HRP, and Amersham ECL Western Blotting Detection Reagents (GE Healthcare) were used for detection.

Affinity purification assays

Approximately 2×10^6 HEK 293T cells were transfected with pcDNA-PB1, pcDNA-PB2, pcDNA-PA and pCAGGS-huANP32A-Strep. 48 h after transfection, cells were lysed in 500 μ l of lysis buffer (50 mM Tris-HCl pH 8.0, 200 mM NaCl, 25% glycerol, 0.5% Igepal CA-630, 1 mM DTT, 1 mM PMSF, 1 \times complete EDTA-free protease inhibitor cocktail tablet (Roche)) for 1 h at 4 °C and cellular debris was cleared by centrifugation for 5 min at 17,000g. The supernatant was diluted in 2 ml 150 mM NaCl and incubated with Strep-Tactin beads (IBA) for 2 h at 4 °C. Beads were washed

three times in wash buffer (10 mM Tris-HCl pH 8.0, 150 mM NaCl, 10% glycerol, 0.1% Igepal CA-630, 1 mM PMSF) and complexes were eluted in 1 \times buffer E (IBA) for 16 h at 4 °C. Eluted complexes were analysed by 12% SDS PAGE and western blotting.

crNA-encapsidation assays

crNA-encapsidation assays were performed as described previously²⁷. In brief, approximately 1×10^6 HEK 293T cells were transfected with pcDNA-PB1a, pcDNA-PB2, pcDNA-PA and pcDNA-NP using Lipofectamine 2000 according to the manufacturer's instructions. Forty-eight hours after transfection, culture medium was replaced with DMEM containing 0.5% FBS and 5 μ g ml⁻¹ actinomycin D and influenza A/WSN/33 virus at multiplicity of infection 5.0. Total cellular RNA was extracted 6 h after infection using Trizol (Sigma) according to the manufacturer's instructions, and viral RNA levels were determined by primer extension analysis as described above.

Reporting summary

Further information on research design is available in the Nature Research Reporting Summary linked to this paper.

Data availability

All data are available from the corresponding authors and/or included in the manuscript or Supplementary Information. Cryo-EM density maps with the corresponding atomic coordinates have been deposited in the Electron Microscopy Data Bank with accession codes EMD-10665 (FluPolC-huANP32A subclass 1), EMD-10667 (FluPolC-huANP32A subclass 2), EMD-10666 (FluPolC-chANP32A subclass 1), EMD-10659 (FluPolC-chANP32A subclass 2), EMD-10662 (FluPolC-chANP32A subclass 3) and EMD-10664 (FluPolC-chANP32A subclass 4), and the Protein Data Bank with accession codes 6XZQ (FluPolC-huANP32A subclass 1), 6Y0C (FluPolC-huANP32A subclass 2), 6XZR (FluPolC-chANP32A subclass 1), 6XZD (FluPolC-chANP32A subclass 2), 6XZG (FluPolC-chANP32A subclass 3) and 6XZP (FluPolC-chANP32A subclass 4).

- Bieniossek, C., Imasaki, T., Takagi, Y. & Berger, I. MultiBac: expanding the research toolbox for multiprotein complexes. *Trends Biochem. Sci.* **37**, 49–57 (2012).
- Zheng, S. Q. et al. MotionCor2: anisotropic correction of beam-induced motion for improved cryo-electron microscopy. *Nat. Methods* **14**, 331–332 (2017).
- Zhang, K. Gctf: Real-time CTF determination and correction. *J. Struct. Biol.* **193**, 1–12 (2016).
- Punjani, A., Rubinstein, J. L., Fleet, D. J. & Brubaker, M. A. cryoSPARC: algorithms for rapid unsupervised cryo-EM structure determination. *Nat. Methods* **14**, 290–296 (2017).
- Scheres, S. H. RELION: implementation of a Bayesian approach to cryo-EM structure determination. *J. Struct. Biol.* **180**, 519–530 (2012).
- Naydenova, K. & Russo, C. J. Measuring the effects of particle orientation to improve the efficiency of electron cryomicroscopy. *Nat. Commun.* **8**, 629 (2017).
- Tan, Y. Z. et al. Addressing preferred specimen orientation in single-particle cryo-EM through tilting. *Nat. Methods* **14**, 793–796 (2017).
- Petterson, E. F. et al. UCSF Chimera—a visualization system for exploratory research and analysis. *J. Comput. Chem.* **25**, 1605–1612 (2004).
- Emstey, P., Lohkamp, B., Scott, W. G. & Cowtan, K. Features and development of Coot. *Acta Crystallogr. D* **66**, 486–501 (2010).
- Jakobi, A. J., Wilmanns, M. & Sachse, C. Model-based local density sharpening of cryo-EM maps. *eLife* **6**, e27131 (2017).
- Burnley, T. Introducing the Proceedings of the CCP-EM Spring Symposium. *Acta Crystallogr. D* **73**, 467–468 (2017).
- Adams, P. D. et al. PHENIX: a comprehensive Python-based system for macromolecular structure solution. *Acta Crystallogr. D* **66**, 213–221 (2010).
- Davis, I. W. et al. MolProbity: all-atom contacts and structure validation for proteins and nucleic acids. *Nucleic Acids Res.* **35**, W375–W383 (2007).
- Waterhouse, A. et al. SWISS-MODEL: homology modelling of protein structures and complexes. *Nucleic Acids Res.* **46** (W1), W296–W303 (2018).
- Crescenzo-Chaigne, B., Naffakh, N. & van der Werf, S. Comparative analysis of the ability of the polymerase complexes of influenza viruses type A, B and C to assemble into functional RNPs that allow expression and replication of heterotypic model RNA templates in vivo. *Virology* **265**, 342–353 (1999).
- Tang, Y. S., Lo, C. Y., Mok, C. K., Chan, P. K. & Shaw, P. C. The extended C-terminal region of influenza C virus nucleoprotein is important for nuclear import and ribonucleoprotein activity. *J. Virol.* **93**, e02048-18 (2019).
- Fodor, E. et al. A single amino acid mutation in the PA subunit of the influenza virus RNA polymerase inhibits endonucleolytic cleavage of capped RNAs. *J. Virol.* **76**, 8989–9001 (2002).

53. Fodor, E. et al. Rescue of influenza A virus from recombinant DNA. *J. Virol.* **73**, 9679–9682 (1999).
54. Paterson, D., te Velthuis, A. J., Vreede, F. T. & Fodor, E. Host restriction of influenza virus polymerase activity by PB2 627E is diminished on short viral templates in a nucleoprotein-independent manner. *J. Virol.* **88**, 339–344 (2014).
55. Robb, N. C., Smith, M., Vreede, F. T. & Fodor, E. NS2/NEP protein regulates transcription and replication of the influenza virus RNA genome. *J. Gen. Virol.* **90**, 1398–1407 (2009).
56. Deng, T. et al. Role of ran binding protein 5 in nuclear import and assembly of the influenza virus RNA polymerase complex. *J. Virol.* **80**, 11911–11919 (2006).
57. Vreede, F. T. & Brownlee, G. G. Influenza virion-derived viral ribonucleoproteins synthesize both mRNA and cRNA in vitro. *J. Virol.* **81**, 2196–2204 (2007).
58. Schneider, C. A., Rasband, W. S. & Eliceiri, K. W. NIH Image to ImageJ: 25 years of image analysis. *Nat. Methods* **9**, 671–675 (2012).
59. Engelhardt, O. G., Smith, M. & Fodor, E. Association of the influenza A virus RNA-dependent RNA polymerase with cellular RNA polymerase II. *J. Virol.* **79**, 5812–5818 (2005).
60. Robert, X. & Gouet, P. Deciphering key features in protein structures with the new ENDscript server. *Nucleic Acids Res.* **42**, W320–W324 (2014).

Acknowledgements We thank N. Naffakh, P.-C. Shaw, G. G. Brownlee and F. Vreede for plasmids; I. Berger for the MultiBac system; D. Karia, A. Howe and D. Clare for assistance with cryo-EM; and G. G. Brownlee and members of the Fodor and Grimes laboratories for helpful comments and discussions. This work was supported by Medical Research Council (MRC) programme grant MR/R009945/1 (to E.F.), Wellcome Investigator Awards 200835/Z/16/Z (to J.M.G.) and 205100/Z/16/Z (to W.S.B.), MRC Studentship (to A.P.W.) and Imperial College President's PhD Scholarship (to E.S.). We thank Diamond Light source for access and support of the cryo-EM facilities at the UK national Electron Bio-Imaging Centre (eBIC) (proposal

EM20223), funded by the Wellcome, MRC and BBSRC. Further electron microscopy provision was provided through the OPIC electron microscopy facility, which was funded by a Wellcome JIF award (060208/Z/00/Z) and is supported by a Wellcome equipment grant (093305/Z/10/Z). Computation was performed at the Oxford Biomedical Research Computing (BMRC) facility, a joint development between the Wellcome Centre for Human Genetics and the Big Data Institute supported by Health Data Research UK and the NIHR Oxford Biomedical Research Centre. The views expressed are those of the author(s) and not necessarily those of the NHS, the NIHR or the Department of Health. Part of this work was supported by Wellcome administrative support grant (203141/Z/16/Z).

Author contributions L.C., H.F., A.P.W., J.R.K., E.F. and J.M.G. conceived and designed the study. H.F., L.C. and J.R.K. carried out cloning of recombinant baculoviruses and protein purification, collected and processed electron microscopy data and built and refined models. A.P.W. and J.S. performed functional assays and analysed data. E.S. and W.S.B. provided plasmids and cell lines. J.M.G. and E.F. supervised the structural and functional studies, respectively. L.C., H.F., A.P.W., J.R.K., E.F. and J.M.G. wrote the manuscript with input from all co-authors.

Competing interests The authors declare no competing interests.

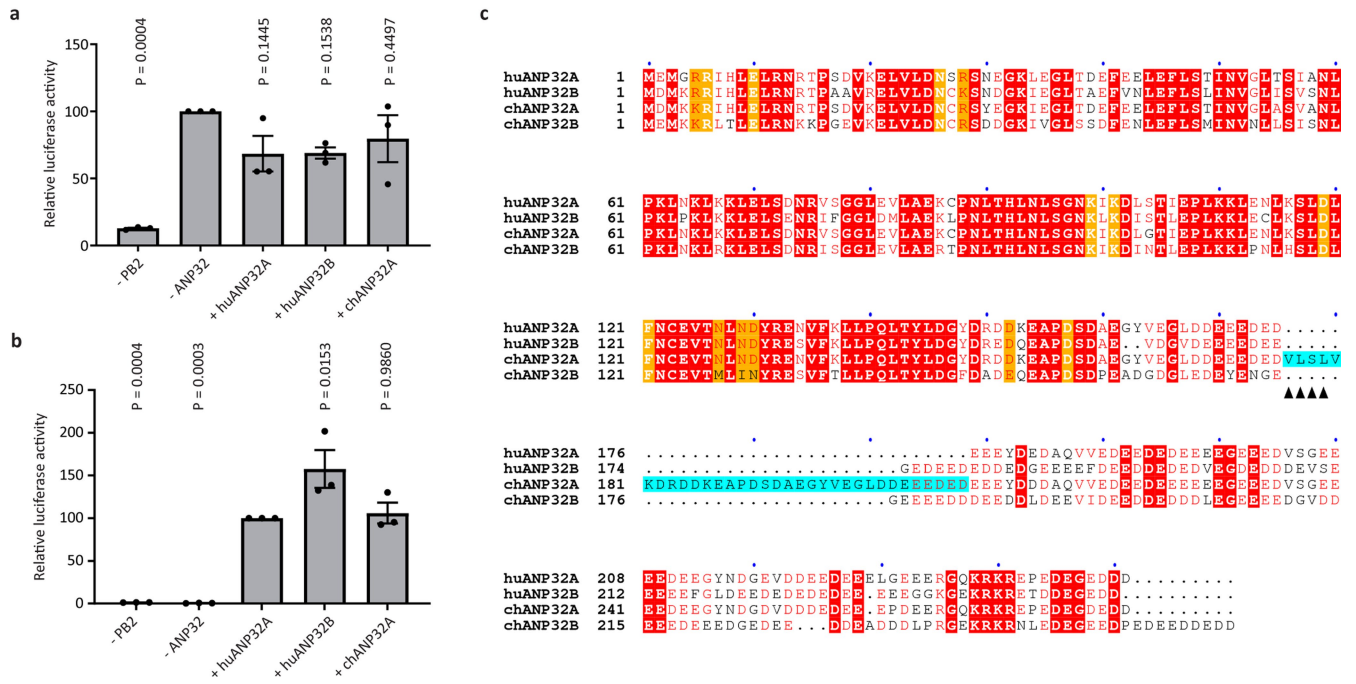
Additional information

Supplementary information is available for this paper at <https://doi.org/10.1038/s41586-020-2927-z>.

Correspondence and requests for materials should be addressed to E.F. or J.M.G.

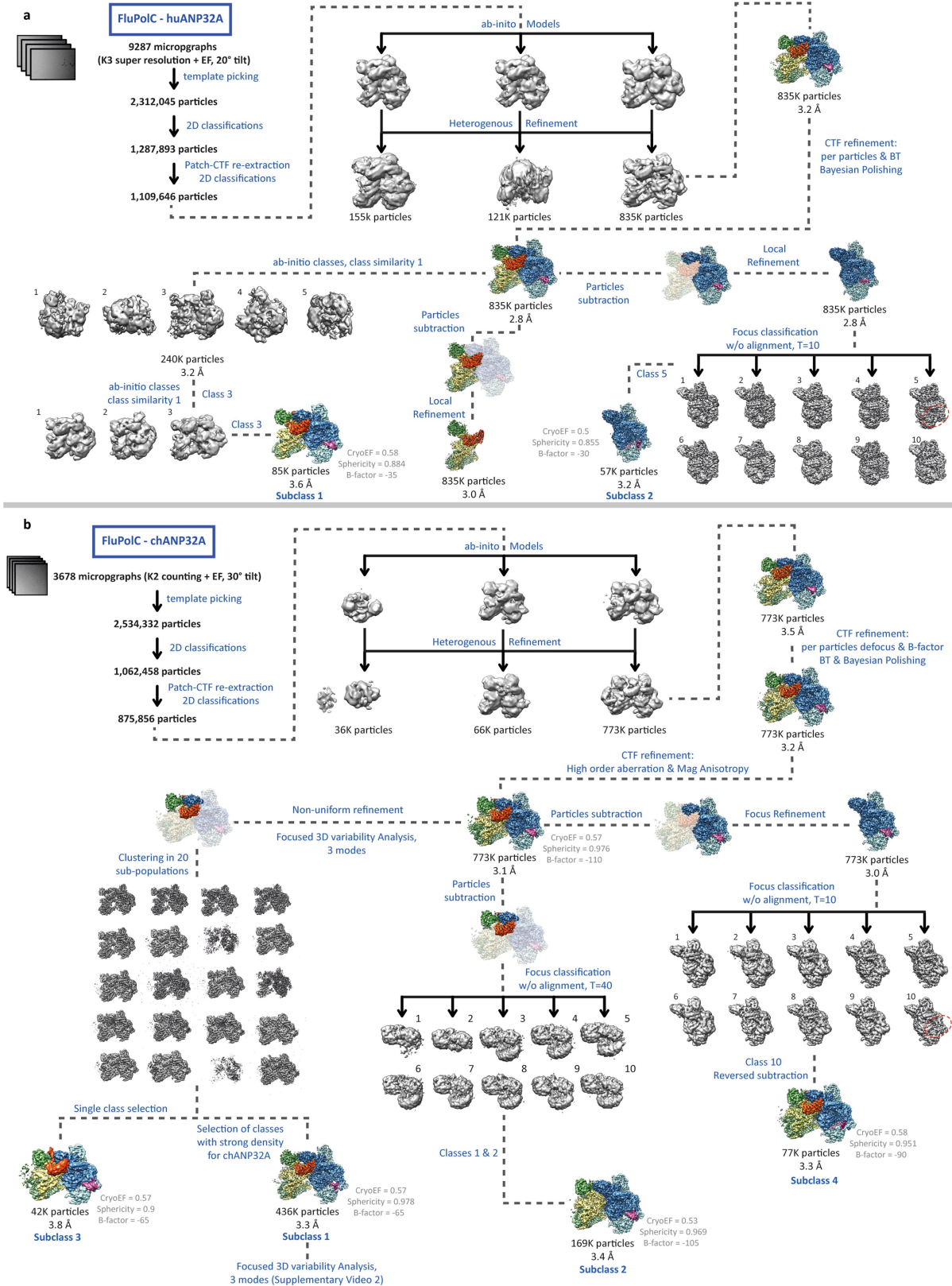
Peer review information *Nature* thanks Julien Lescar, Yi Shi, Xiu-Feng Wan and the other, anonymous, reviewer(s) for their contribution to the peer review of this work. Peer reviewer reports are available.

Reprints and permissions information is available at <http://www.nature.com/reprints>.



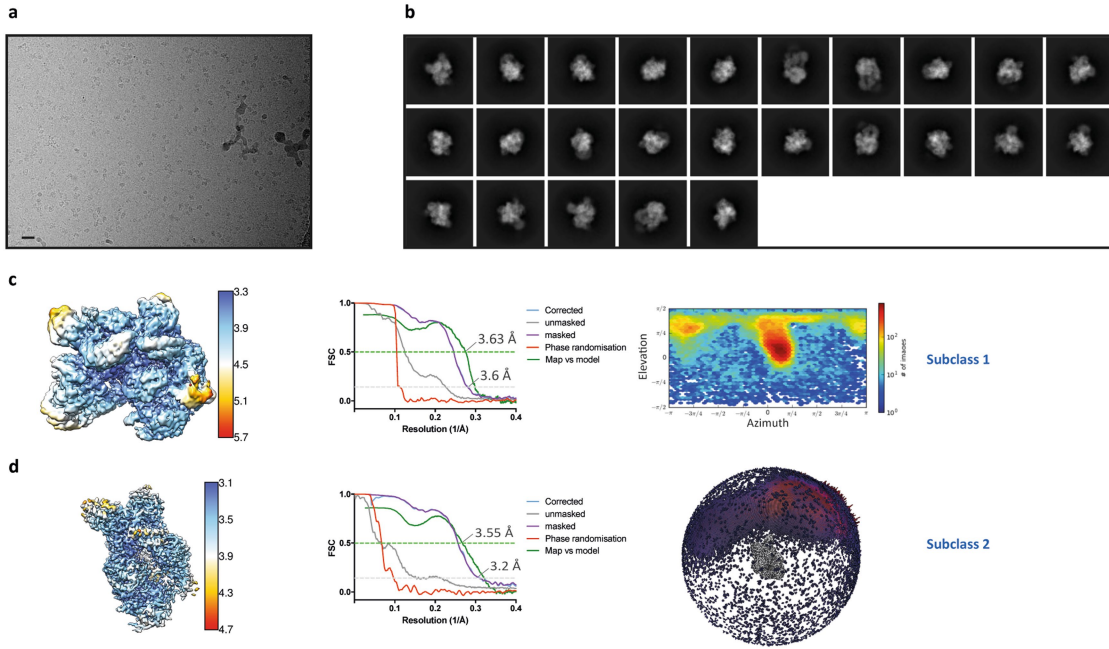
Extended Data Fig. 1 | FluPoIC activity depends on ANP32A and alignment of ANP32 proteins. a, b, Luciferase reporter gene activities reflecting FluPoIC activity in control (a) and dKO (b) eHAP cells in the presence or absence of overexpressed huANP32A, huANP32B or chANP32A. Data are presented as mean values \pm s.e.m. $n = 3$ biologically independent samples from $n = 3$ independent experiments. Ordinary one-way ANOVA with Dunnett's post hoc

test for multiple comparisons. $P < 0.05$ is considered significant to reject the null hypothesis. c, Sequence alignment of huANP32A, huANP32B, chANP32A, chANP32B. Residues involved in hydrogen bonding interactions with FluPoIC are indicated in orange. The chANP32A avian-specific 33 amino acid insertion is highlighted in cyan. The SUMO interaction motif (SIM) sequence is indicated by black triangles. The figure was prepared with Esprnt 3.0⁶⁰.

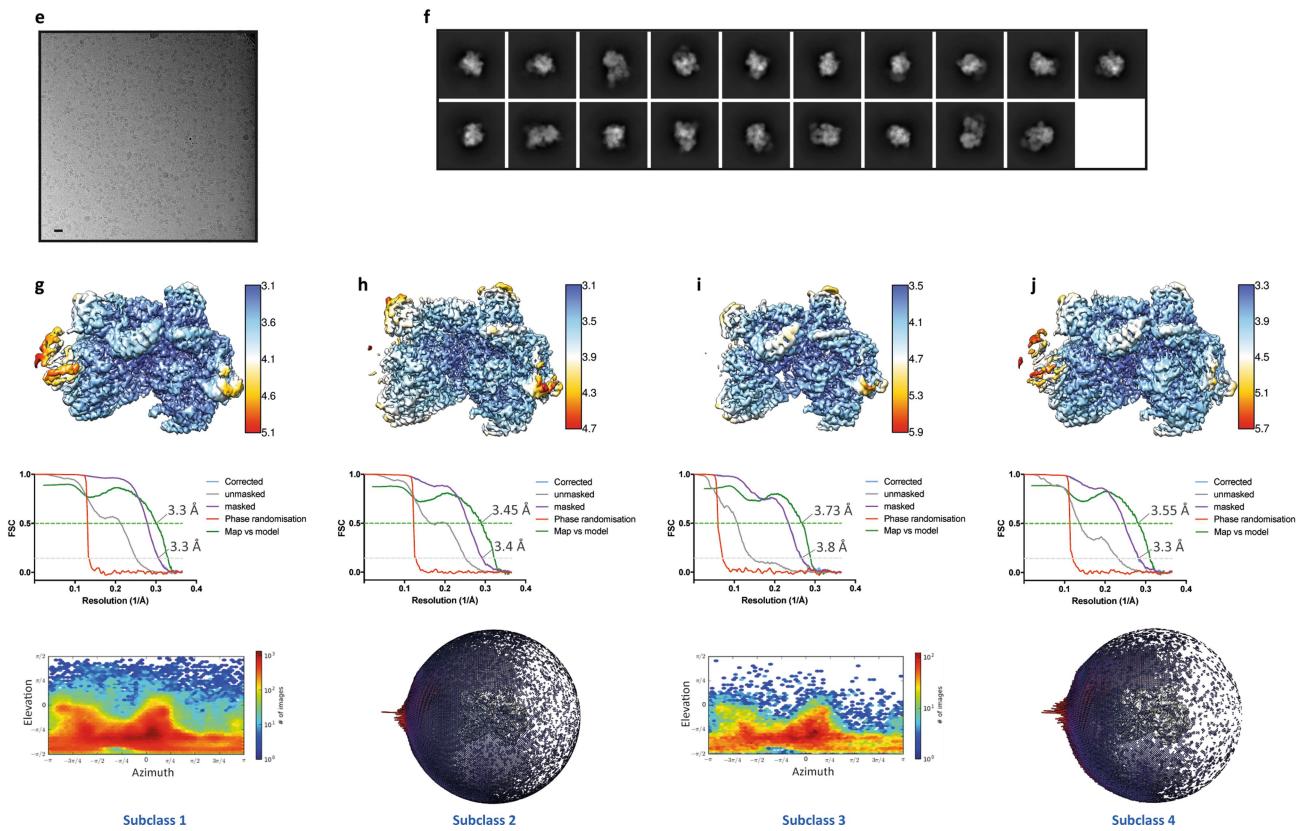


Extended Data Fig. 2 | Data collection, processing and analysis scheme. a, b, Flowchart for the processing and the classification of the FluPoIC-huANP32A complex (a) and FluPoIC-chANP32A complex (b).

FluPoIC - huANP32A



FluPoIC - chANP32A

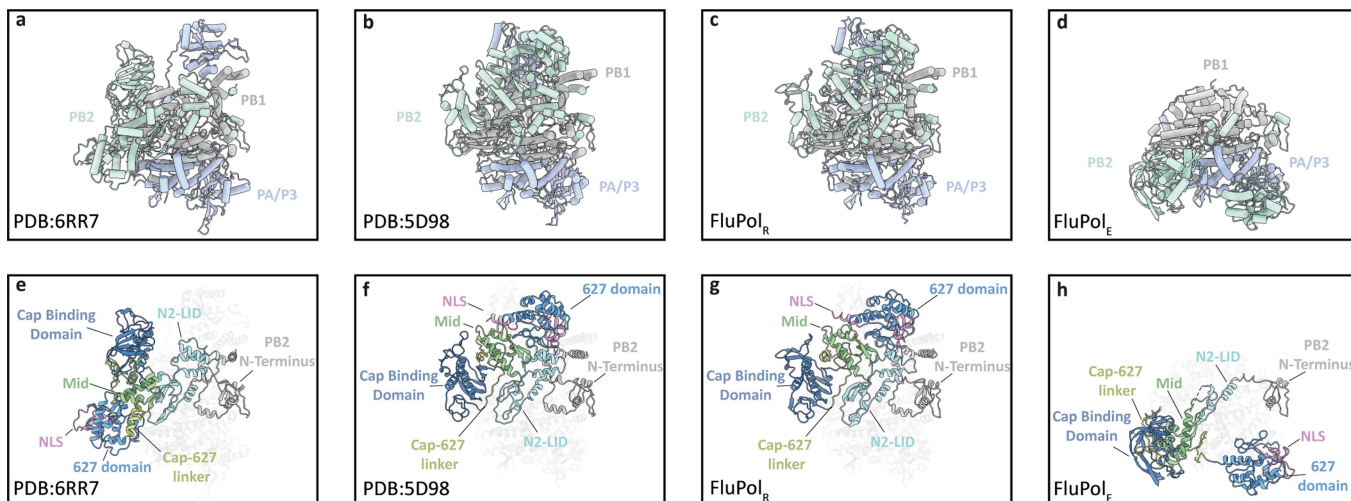


Extended Data Fig. 3 | See next page for caption.

Article

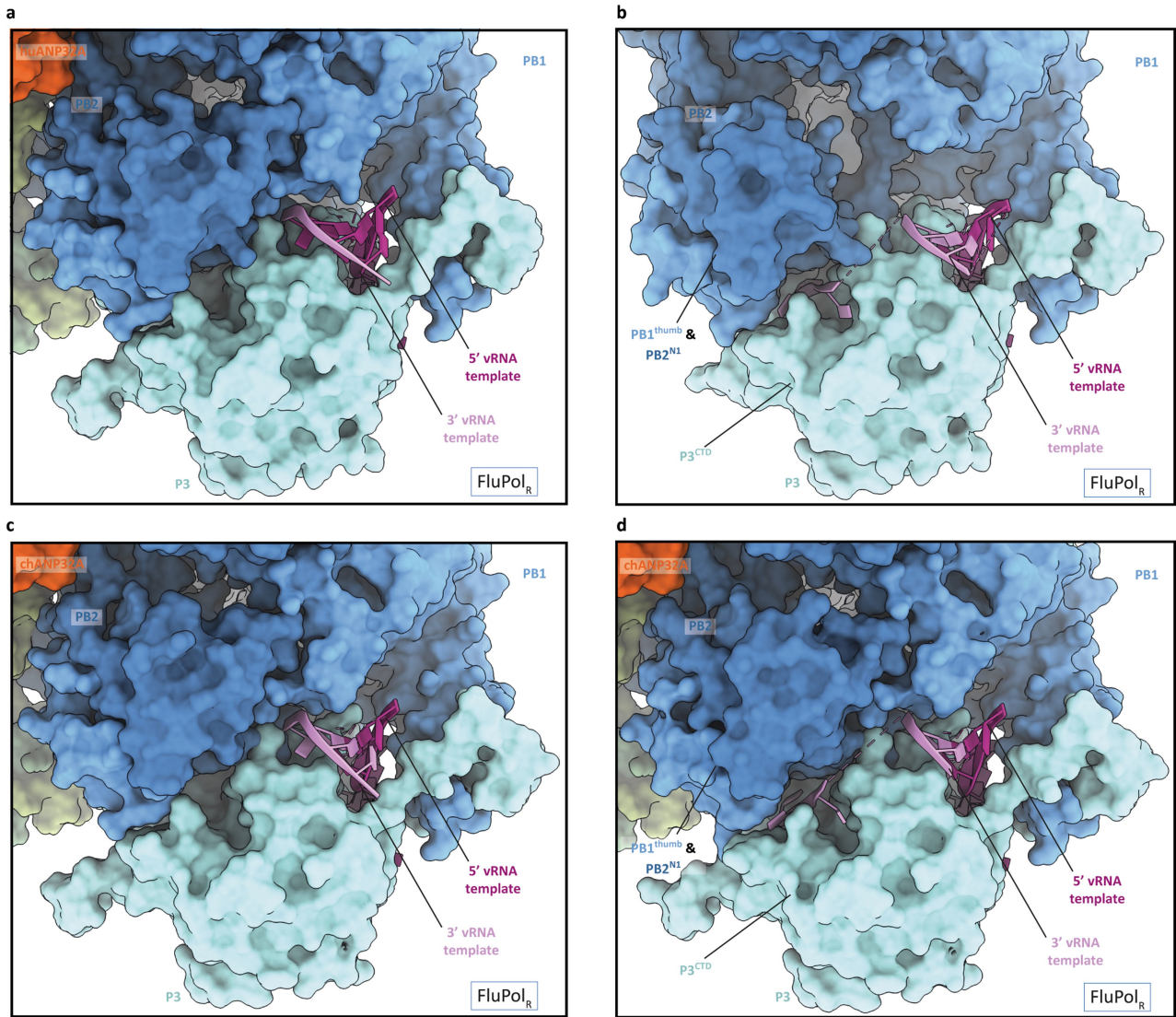
Extended Data Fig. 3 | Single-particle cryo-EM analysis of FluPolC-huANP32A and FluPolC-chANP32A complexes. **a, e**, Representative micrograph of FluPolC-huANP32A (**a**) and FluPolC-chANP32A (**e**) embedded in vitreous ice. Scale bar, 200 Å. **b, f**, Representative 2D class averages of FluPolC-huANP32A (**b**) and FluPolC-chANP32A (**f**). **c, d**, Data analysis for FluPolC-huANP32A Subclass1 (**c**) and Subclass2 (**d**). 3D reconstruction locally filtered and coloured according to RELION local resolution (left panel). FSC curve indicating overall map resolution and model-to-map FSC (middle panel). Curves are shown for phase randomization, unmasked, masked and phase-

randomization-corrected masked maps. Angular distribution of particle projections with the cryo-EM map shown in grey (right panel). **g-j**, Data analysis for FluPolC-chANP32A Subclass1 (**g**), Subclass2 (**h**), Subclass3 (**i**) and Subclass4 (**j**). 3D reconstruction locally filtered and coloured according to RELION local resolution (top panel). FSC curve indicating overall map resolution and the model-to-map FSC (middle panel). Curves are shown for phase randomization, unmasked, masked and phase-randomization-corrected masked maps. Angular distribution of particle projections with the cryo-EM map shown in grey (bottom panel).



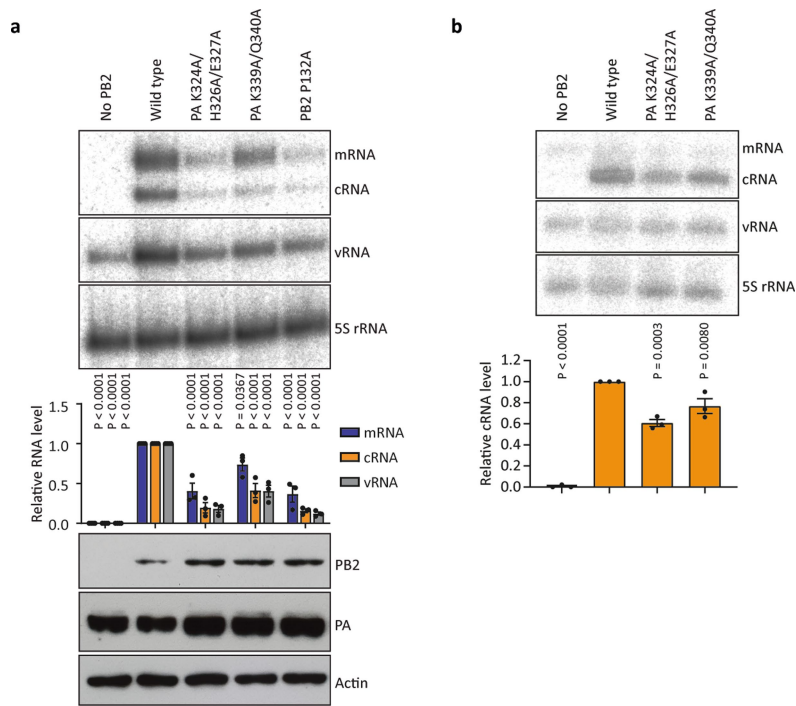
Extended Data Fig. 4 | Comparison of FluPol_R and FluPol_E structures with the transcriptase and apo conformations of FluPol. **a–d**, Comparison of structures of human influenza A/NT/60/68 (H3N2) bound to vRNA and capped RNA in the transcriptase conformation (PDB: 6RR7) (**a**) and human influenza

C/Johannesburg/1/66 in the apo conformation (PDB: 5D98) (**b**) with structures of FluPol_R (**c**) and FluPol_E (**d**) in the FluPolC-chANP32A complex. **e–h**, Comparison of the PB2 domain arrangements in the complexes shown in **a–d**.



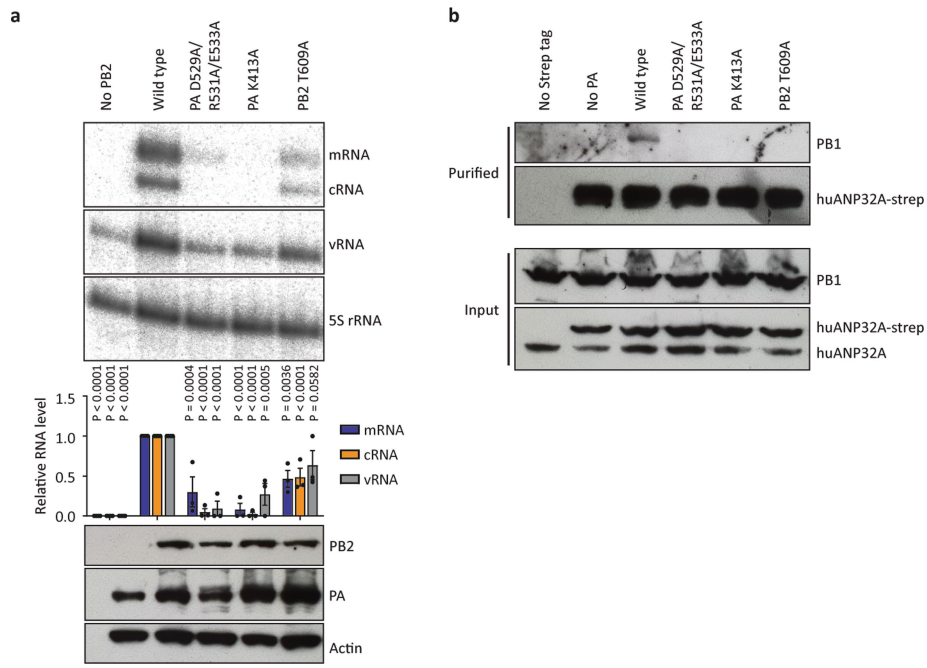
Extended Data Fig. 5 | Close-up view of the interaction of 5' and 3' vRNA termini with FluPol_R. **a, c**, Close-up view of the 3' vRNA pointing towards the active site in the FluPolC-huANP32A (**a**) and FluPolC-chANP32A (**c**) structures.

b, d, Close-up view of the 3' vRNA binding in a groove located between P3^{CTD} and the PB1^{thumb} and PB2^{NI} subdomains in the FluPolC-huANP32A (**b**) and FluPolC-chANP32A (**d**) structures.



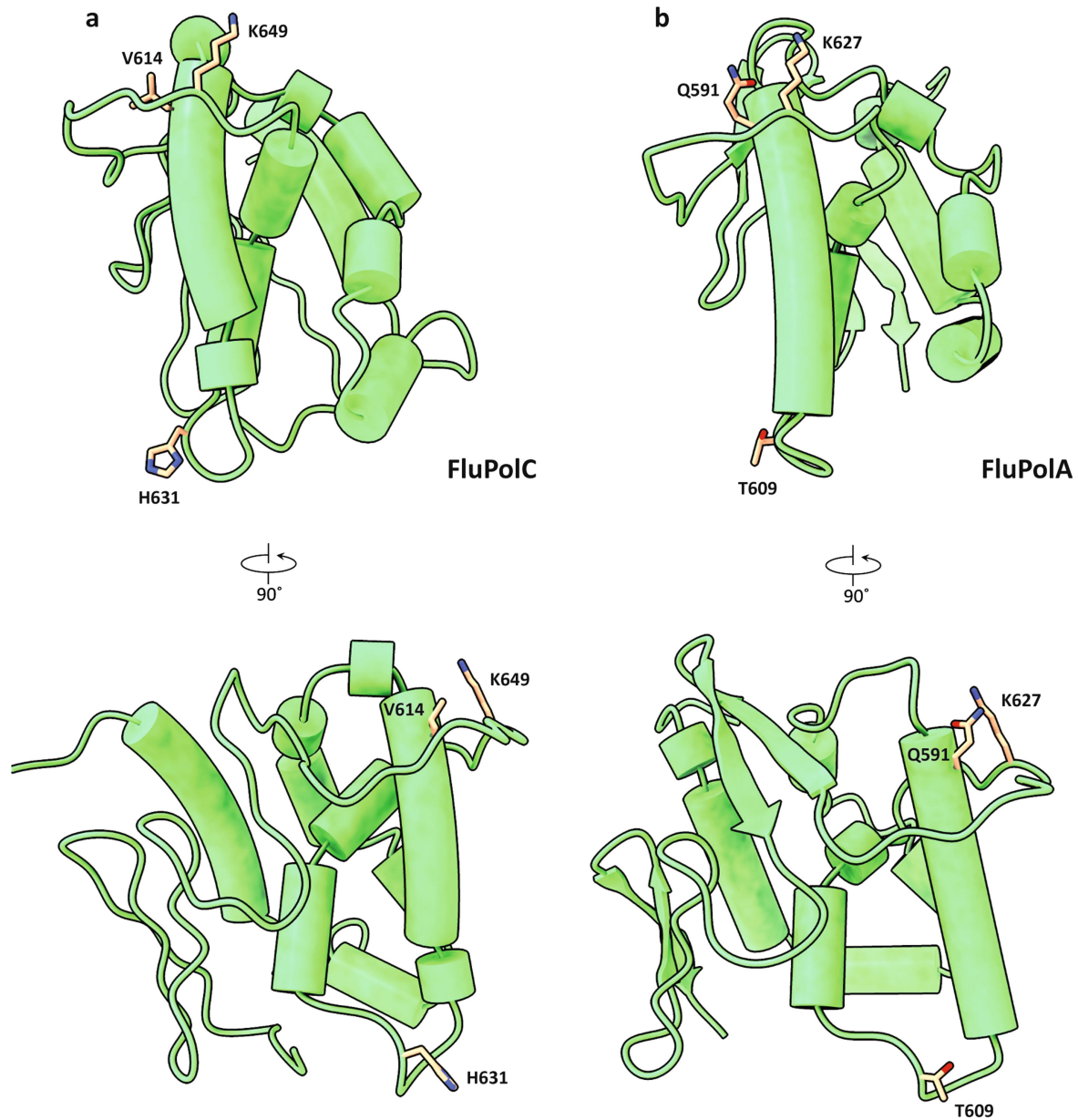
Extended Data Fig. 6 | Effect of FluPol_r-FluPol_E dimer interface mutations on FluPolA activity. a, b, Effect of mutations at the FluPol_r-FluPol_E dimer interface on FluPolA activity in viral minigenome assays (a) and cRNA encapsidation by FluPolA (b). Data are presented as mean values ± s.e.m. $n = 3$ biologically independent samples from $n = 3$ independent experiments.

Ordinary one-way ANOVA with Dunnett's post hoc test for multiple comparisons. $P < 0.05$ is considered significant to reject the null hypothesis. Western blot analyses were repeated from $n = 3$ independent experiments with similar results. For gel source data, see Supplementary Fig. 2.



Extended Data Fig. 7 | Effect of FluPoIA mutations at the FluPoIA-ANP32A interface on FluPoIA activity and interaction with huANP32A. a, b, Effect of FluPoIA mutations at the FluPoIA-ANP32A interface on FluPoIA activity in viral minigenome assays on (a) and FluPoIA-ANP32A interaction (b). Data are presented as mean values \pm s.e.m. $n = 3$ biologically independent samples from

$n = 3$ independent experiments. Ordinary one-way ANOVA with Dunnett's post hoc test for multiple comparisons. $P < 0.05$ is considered significant to reject the null hypothesis. Western blot analyses were repeated from $n = 3$ independent experiments with similar results. For gel source data, see Supplementary Fig. 2.



Extended Data Fig. 8 | Structural comparison of PB2⁶²⁷ domains of FluPoIA and FluPoIC. Structures of the PB2⁶²⁷ domains from crystal structures of FluPoI from influenza C/Johannesburg/1/1966 (a, PDB ID: 5D98) and A/NT/60/1968

(H3N2) (b, PDB ID: 6QNW) viruses are aligned and shown in cartoon mode. Residues discussed in this study are highlighted in stick mode and coloured in orange.

Article

Extended Data Table 1 | Cryo-EM data collection, refinement and validation statistics

	FluPol _c -huANP32			FluPol _c -chANP32		
	Sub-Class1	Sub-Class2	Sub-Class1	Sub-Class2	Sub-Class3	Sub-Class4
	EMD-10665	EMD-10667	EMD-10666	EMD-10659	EMD-10662	EMD-10664
	6XZQ	6Y0C	6XZR	6XZD	6XZG	6XZP
Data collection						
Microscope	Titan Krios IV (eBIC)			Titan Krios (Strubi)		
Voltage (kV)	300			300		
Detector	Gatan K3 with EF			Gatan K2 with EF		
Recording mode	Super Resolution			Counting		
Magnification	81,000			105,000		
Movie/micrograph pixel size (Å)	0.5425			1.37		
Dose rate (e-/Å ² /sec)	16			3.53		
Number of frames per movie	30			44		
Movie exposure time (s)	2			11		
Total dose (e-/Å ²)	32.1			38.8		
Defocus range (um)	-2 to -3.5			-2 to -3.5		
Volta Phase Plate	no			no		
EM data processing						
Number of movies/micrographs	9287			3678		
Box size (px)	300	450		280		
Particle number (total)	2,312,045			2,534,332		
Particle number (post 2D)	846,766			875,856		
Particle number (post 3D)	835,000			773,000		
Particle number (used in final map)	85,000	57,000	349K	169K	77K	71K
Symmetry	C1	C1	C1	C1	C1	C1
Map resolution (FSC 0.143)	3.6	3.2	3.3	3.4	3.8	3.3
Local resolution range (FSC 0.5)	3.3 - 5.7	3.1 - 4.7	3.1 - 5.7	3.1 - 4.7	3.5 - 5.9	3.3 - 5.7
Map sharpening B-factor (Å ²)	-35	-30	-65	-105	-65	-90
Model Building and Validation						
Initial model used	6XZR	6XZR	5D98, 6RR7, 4XOS	6XZR	6XZR	6XZR
Model composition						
Non-hydrogen protein atoms	56895	34969	66214	63743	66001	66227
Protein residues	3492	2135	4077	3919	4065	4077
Nucleotides (RNA)	19	20	19	20	19	20
RMSD from ideal						
Bond length (Å)	0.005	0.006	0.006	0.003	0.005	0.005
Bond angles (°)	0.638	0.679	0.576	0.53	0.695	0.749
Validation						
Molprobrity score	1.74	1.96	1.74	1.82	1.82	1.87
Clashscore	5.76	6.1	6.47	7.81	7.75	8.67
Rotamers outliers (%)	1.26	2.2	0.83	0.26	0.92	0.17
FSC (0.5) model-vs-map	3.63	3.68	3.3	3.45	3.73	3.55
CC model-vs-map (masked)	0.73	0.76	0.81	0.75	0.78	0.78
Ramachandran plot						
Favored (%)	95	94.84	94.32	94.27	94.12	93.92
Allowed (%)	5	5.16	5.68	5.73	5.88	6.08
Outliers (%)	0	0	0	0	0	0

Reporting Summary

Nature Research wishes to improve the reproducibility of the work that we publish. This form provides structure for consistency and transparency in reporting. For further information on Nature Research policies, see [Authors & Referees](#) and the [Editorial Policy Checklist](#).

Statistics

For all statistical analyses, confirm that the following items are present in the figure legend, table legend, main text, or Methods section.

n/a Confirmed

- | | | |
|-------------------------------------|-------------------------------------|--|
| <input type="checkbox"/> | <input checked="" type="checkbox"/> | The exact sample size (n) for each experimental group/condition, given as a discrete number and unit of measurement |
| <input type="checkbox"/> | <input checked="" type="checkbox"/> | A statement on whether measurements were taken from distinct samples or whether the same sample was measured repeatedly |
| <input type="checkbox"/> | <input checked="" type="checkbox"/> | The statistical test(s) used AND whether they are one- or two-sided
<i>Only common tests should be described solely by name; describe more complex techniques in the Methods section.</i> |
| <input checked="" type="checkbox"/> | <input type="checkbox"/> | A description of all covariates tested |
| <input checked="" type="checkbox"/> | <input type="checkbox"/> | A description of any assumptions or corrections, such as tests of normality and adjustment for multiple comparisons |
| <input type="checkbox"/> | <input checked="" type="checkbox"/> | A full description of the statistical parameters including central tendency (e.g. means) or other basic estimates (e.g. regression coefficient) AND variation (e.g. standard deviation) or associated estimates of uncertainty (e.g. confidence intervals) |
| <input type="checkbox"/> | <input checked="" type="checkbox"/> | For null hypothesis testing, the test statistic (e.g. F , t , r) with confidence intervals, effect sizes, degrees of freedom and P value noted
<i>Give P values as exact values whenever suitable.</i> |
| <input checked="" type="checkbox"/> | <input type="checkbox"/> | For Bayesian analysis, information on the choice of priors and Markov chain Monte Carlo settings |
| <input checked="" type="checkbox"/> | <input type="checkbox"/> | For hierarchical and complex designs, identification of the appropriate level for tests and full reporting of outcomes |
| <input checked="" type="checkbox"/> | <input type="checkbox"/> | Estimates of effect sizes (e.g. Cohen's d , Pearson's r), indicating how they were calculated |

Our web collection on [statistics for biologists](#) contains articles on many of the points above.

Software and code

Policy information about [availability of computer code](#)

Data collection

FEI EPU 2.1 and SerialEM 3.7

Data analysis

PHENIX 1.17, Coot 0.9, MotionCor2.1.1, Gctf-v.1.06, RELION 3.1, cryoSPARC V2.12, Chimera 1.13, MolProbity 4.5, GraphPad Prism 7, 3D FSC, CryoEF 1.1, ImageJ 1.52p, CCP-EM 1.4, LocScale

For manuscripts utilizing custom algorithms or software that are central to the research but not yet described in published literature, software must be made available to editors/reviewers. We strongly encourage code deposition in a community repository (e.g. GitHub). See the Nature Research [guidelines for submitting code & software](#) for further information.

Data

Policy information about [availability of data](#)

All manuscripts must include a [data availability statement](#). This statement should provide the following information, where applicable:

- Accession codes, unique identifiers, or web links for publicly available datasets
- A list of figures that have associated raw data
- A description of any restrictions on data availability

Cryo-EM density maps with the corresponding atomic coordinates have been deposited in the Electron Microscopy Data Bank and the Protein Data Bank, respectively, with accession codes EMD-10665, PDB ID 6XZQ (FluPolC-huANP32A-subclass 1), EMD-10667, PDB ID 6Y0C (FluPolC-huANP32A-subclass 2), EMD-10666, PDB ID 6XZR (FluPolC-chANP32A-subclass 1), EMD-10659, PDB ID 6XZD (FluPolC-chANP32A-subclass 2), EMD-10662, PDB ID 6XZG (FluPolC-chANP32A-subclass 3), EMD-10664, PDB ID 6XZP (FluPolC-chANP32A-subclass 4).

Field-specific reporting

Please select the one below that is the best fit for your research. If you are not sure, read the appropriate sections before making your selection.

- Life sciences Behavioural & social sciences Ecological, evolutionary & environmental sciences

For a reference copy of the document with all sections, see [nature.com/documents/nr-reporting-summary-flat.pdf](https://www.nature.com/documents/nr-reporting-summary-flat.pdf)

Life sciences study design

All studies must disclose on these points even when the disclosure is negative.

Sample size	Sample sizes were estimated on the basis of previous studies using similar methods and analyses that are widely published; see Deng et al. J Virol. 2006 (https://jvi.asm.org/content/80/24/11911), Vreede et al. J Virol. 2007 (https://jvi.asm.org/content/81/5/2196), Fan et al. Nature 2019 (https://www.nature.com/articles/s41586-019-1530-7) as examples.
Data exclusions	Following the first steps of cryo-EM data processing, a small number of the acquired cryo-EM movies were discarded owing to poor ice quality, excessive movement or defocus. Otherwise no data were excluded.
Replication	All functional assays of FluPoLA and FluPoLC were carried out at least three times. All attempts to replicate data were successful.
Randomization	Randomization is not relevant to our study, as samples were not assigned to experimental groups and data were collected and processed according to standard techniques for cryoEM, protein and RNA analysis.
Blinding	Blinding was not relevant in this study, because all the data were analyzed using unbiased methods.

Reporting for specific materials, systems and methods

We require information from authors about some types of materials, experimental systems and methods used in many studies. Here, indicate whether each material, system or method listed is relevant to your study. If you are not sure if a list item applies to your research, read the appropriate section before selecting a response.

Materials & experimental systems

n/a	Involved in the study
<input type="checkbox"/>	<input checked="" type="checkbox"/> Antibodies
<input type="checkbox"/>	<input checked="" type="checkbox"/> Eukaryotic cell lines
<input checked="" type="checkbox"/>	<input type="checkbox"/> Palaeontology
<input checked="" type="checkbox"/>	<input type="checkbox"/> Animals and other organisms
<input checked="" type="checkbox"/>	<input type="checkbox"/> Human research participants
<input checked="" type="checkbox"/>	<input type="checkbox"/> Clinical data

Methods

n/a	Involved in the study
<input checked="" type="checkbox"/>	<input type="checkbox"/> ChIP-seq
<input checked="" type="checkbox"/>	<input type="checkbox"/> Flow cytometry
<input checked="" type="checkbox"/>	<input type="checkbox"/> MRI-based neuroimaging

Antibodies

Antibodies used	Rabbit anti-PB1 (Genetex, GTX125923); Rabbit anti-PB2 (Genetex, GTX125925); Rabbit anti-actin (Sigma, A2066); Rabbit anti-ANP32A (Sigma, AV40203); Goat anti-rabbit IgG peroxidase conjugate (Sigma, A 8275); Rabbit anti-PA (custom)
Validation	Commercially available antibodies were validated by suppliers. Rabbit anti-PB1 (Genetex, GTX125923) https://www.genetex.com/Product/Detail/Influenza-A-virus-PB1-protein-antibody/GTX125923#datasheet Rabbit anti-PB2 (Genetex, GTX125925) https://www.genetex.com/Product/Detail/Influenza-A-virus-PB2-protein-antibody/GTX125925 Rabbit anti-actin (Sigma, A2066) https://www.sigmaaldrich.com/catalog/product/sigma/a2066?lang=en&region=GB Rabbit anti-ANP32A (Sigma, AV40203) https://www.sigmaaldrich.com/catalog/product/sigma/av40203?lang=en&region=GB Goat anti-rabbit IgG peroxidase conjugate (Sigma, A 8275) https://www.sigmaaldrich.com/catalog/product/sigma/a8275?lang=en&region=GB Rabbit anti-PA was validated in the original publication; see Engelhardt et al. J. Virol. 2005 (https://jvi.asm.org/content/79/9/5812)

Eukaryotic cell lines

Policy information about [cell lines](#)

Cell line source(s)	Human embryonic kidney (HEK) 293T and Sf9 insect cells were sourced from the Cell Bank of the Sir William Dunn School of Pathology, University of Oxford. eHAP cells were purchased from Horizon Discovery.
---------------------	---

Authentication

Authentication was not performed for this study.

Mycoplasma contamination

Mycoplasma testing revealed no contamination.

Commonly misidentified lines
(See [ICLAC](#) register)

No commonly misidentified cell lines were used.